Large nonsaturating magnetoresistance, weak anti-localization, and non-trivial topological states in $SrAl_2Si_2$

Sudip Malick,[1] A. B. Sarkar,[1] Antu Laha,[1] M. Anas,[2] V. K. Malik,[2] Amit Agarwal,[1,*] Z. Hossain,[1,†] and J. Nayak[1,‡]

[1]*Department of Physics, Indian Institute of Technology, Kanpur 208016, India*

[2]*Department of Physics, Indian Institute of Technology Roorkee, Roorkee 247667, India*

(Received 7 April 2021; revised 21 January 2022; accepted 15 July 2022; published 1 August 2022)

We explore the electronic and topological properties of single-crystal $SrAl_2Si_2$ using magnetotransport experiments in conjunction with first-principle calculations. We find that the temperature-dependent resistivity shows a pronounced peak ∼50 K. We observe several remarkable features at low temperatures such as large nonsaturating magnetoresistance (MR), Shubnikov–de Haas oscillations and cusplike magnetoconductivity (MC) . The maximum value of MR turns out to be 459% at 2 K and 12 T. The analysis of the cusplike feature in MC indicates a clear signature of weak anti-localization. Our Hall resistivity measurements confirm the presence of two types of charge carriers in $SrAl_2Si_2$ with low carrier density.

DOI: 10.1103/PhysRevB.106.075105

I. INTRODUCTION

The paradigm of topology in crystalline materials has brought relativistic physics to tabletop experiments. Current understanding of topological band theory and crystalline symmetries has led to the realization of several topological materials with bulk and surface properties, giving rise to exciting physics and functionalities. Their exotic bulk and surface electronic structures can give rise to interesting transport phenomena such as extremely large magnetoresistance (MR), chiral anomaly, quantum oscillation, weak anti-localization (WAL) effect, and ultra high mobility [1–10]. Topological semimetals (TSMs) like Dirac [11,12], Weyl, and nodal line semimetals [13] are the consequence of such non-trivial states in which the bulk bands host symmetry-protected gapless states between the valence and conduction bands near the Fermi level.

Recently, materials (122 phase) belonging to the space group $P\bar{3}m1$ (No. 164) have attracted significant interest owing to the existence of diverse topological phases. $EuCd_2As_2$ and $EuCd_2Sb_2$ are the two specific systems in this group where magnetism plays a crucial role in defining their electronic and topological ground states. Depending on the magnetic spin configuration, these systems can either be topological insulators or Dirac semimetals [14–18]. On the other hand, a nonmagnetic compound in the same group $CaAl_2Si_2$ is predicted to host multiple topological states such as topological Dirac nodal lines and type-II Dirac fermions. The inclusion of spin-orbit coupling (SOC) in this system opens up a small gap in the Dirac line nodes, while the crystal symmetries protect the Lorentz symmetry violating tilted Dirac point states [19]. Recently, the topological Dirac semimetallic phase in $CaAl_2Si_2$ has been identified experimentally by Deng *et al.* [20].

Here, we have explored another nonmagnetic system from the same space group ($P\bar{3}m1$) $SrAl_2Si_2$. We report the synthesis of a single crystal of $SrAl_2Si_2$ and present a systematic study of its physical properties by using magnetotransport measurements in conjunction with first-principle calculations. Our magnetotransport measurements show (i) a broad peak in the temperature-dependent resistivity, (ii) large nonsaturating MR up to $B = 12$ Tesla, (iii) quantum oscillations in the conductivity, (iv) WAL, and (v) two-carrier-dependent Hall resistivity which is non-linear in the magnetic field strength. Our density functional theory (DFT)-based calculations clearly indicate the presence of a Dirac point in the electronic dispersion, the existence of interesting surface states at the Fermi energy, and multiple electron and hole pockets at the Fermi energy—consistent with the observed Hall resistivity.

II. METHODS AND CRYSTAL STRUCTURE

Single crystals of $SrAl_2Si_2$ were synthesized by the standard flux method with Al being used as a flux [19]. High-purity elements Sr (99.99%, Alfa Aesar), Al (99.999%, Alfa Aesar), and Si (99.99%, Alfa Aesar) were taken in 1:20:2 molar ratio and mixed in an alumina crucible and then sealed in an evacuated quartz ampule. The whole assembly was heated to 1373 K, maintained at this temperature for 20 h, and then slowly cooled down to 1023 K at a rate of 1.5 K/h. The excess Al flux was removed by centrifuging to extract the single crystals. The typical dimensions of the crystals were $1.5 \times 1 \times 0.5$ mm^3. The crystal structure and the phase purity were determined by x-ray diffraction (XRD) in a PANalytical X'Pert PRO diffractometer with Cu Kα_1 radiation and by energy dispersion x-ray spectroscopy in JEOL JSM-6010LA. Electrical resistivity and magnetotransport measurements were performed by the conventional

*amitag@iitk.ac.in
†zakir@iitk.ac.in
‡jnayak@iitk.ac.in

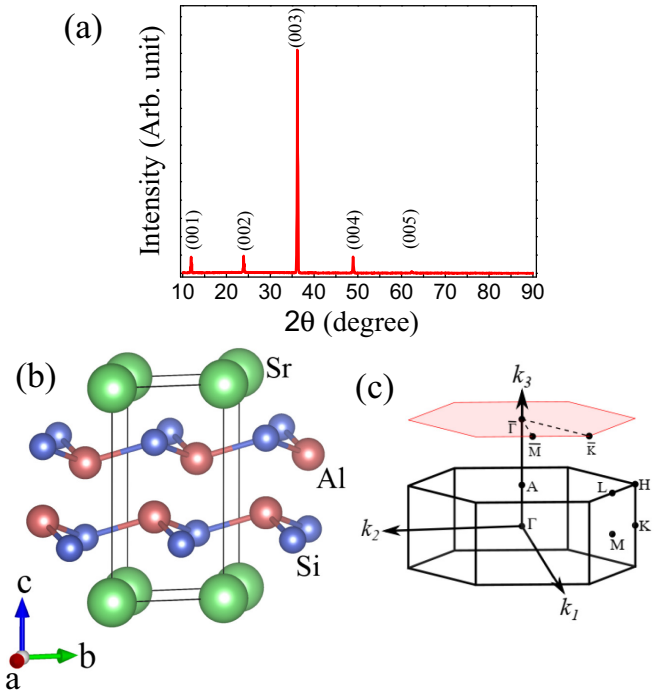

FIG. 1. The crystal structure and Brillouin zone (BZ) of $SrAl_2Si_2$. (a) Single-crystal x-ray diffraction (XRD) pattern of $SrAl_2Si_2$ with sharp peaks confirm the good quality of the single crystals. (b) The schematic representation of the crystal structure along with its unit cell. (c) Bulk and (001) projected hexagonal surface BZ, with the high-symmetry points marked.

four-probe technique in a physical property measurement system (Dynacool PPMS, Quantum Design).

We calculated the electronic structure of $SrAl_2Si_2$ using the framework of DFT as implemented in the Vienna *Ab initio* Simulation Package (VASP) [21,22]. The exchange-correlation effects were treated within the generalized gradient approximation in the form of a Perdew-Burke-Ernzerhof-type exchange-correlation potential [23]. We used the kinetic energy cutoff for the plane-wave basis set as 500 eV and a Γ-centered $9 \times 9 \times 9$ k-mesh to perform the Brillouin zone (BZ) integration [24]. The tight-binding model Hamiltonian was constructed using the VASP2WANNIER90 interface [25]. We used the iterative Green's function method, as implemented in the WANNIERTOOLS package [26] to obtain the surface and bulk spectral function. We plotted the crystal structure using VESTA software.

The single-crystal XRD pattern of $SrAl_2Si_2$ is presented in Fig. 1(a). It crystalizes in a hexagonal structure with space group $P\bar{3}m1$, as shown in Fig. 1(b). The obtained lattice parameters from the Rietveld refinement of the powder XRD data are $a = b = 4.190$ Å and $c = 7.429$ Å, which agree well with the previous report [27]. $SrAl_2Si_2$ is a layered material with Si and Al atoms being arranged in a layer, followed by a layer of Sr atoms. The Sr atoms are situated at the Wyckoff site (0, 0, 0), whereas the Si and Al atoms are situated at $(\frac{1}{3}, \frac{2}{3}, 0.2762)$ and $(\frac{1}{3}, \frac{2}{3}, 0.6245)$, respectively. The structure possesses three- and twofold rotational symmetry along with three vertical mirror planes $\mathcal{M}_{100}$, $\mathcal{M}_{010}$, and $\mathcal{M}_{110}$. We show the bulk BZ along with the projected (001) surface BZ in Fig. 1(c).

III. MAGNETOTRANSPORT

The measured temperature dependence of the longitudinal electrical resistivity (300 to 2 K) is shown in Fig. 2(a). We find that the resistivity increases with the decrease of temperature from 300 K, and it exhibits a broad peak ∼50 K, consistent with earlier reports [27,28]. This is likely a consequence of the thermal activation of the carriers, which manifests as a semiconductor (or semimetal)-like behavior at higher temperature [29]. To estimate the thermally activated effective energy gap or pseudogap, we have performed a linear fit to the resistivity in the Arrhenius plot >100 K, as shown in the inset of Fig. 2(a), and estimated the effective energy gap to be $E_g = 8.4$ meV. Under the application of an external magnetic field, the low-temperature metallic state is gradually suppressed, as shown in Fig. 2(b). Above a certain magnetic field ($B > 1$ T), only semiconducting-like behavior is observed with a resistivity plateau <10 K.

A. MR

Next, we present the MR as a function of the magnetic field at various temperatures in Fig. 2(c). The MR is defined by the following expression:

$$\mathrm{MR}(\%) = \frac{\rho_{xx}(B) - \rho_{xx}(0)}{\rho_{xx}(0)} \times 100\%. \quad (1)$$

Here, $\rho_{xx}(B)$ and $\rho_{xx}(0)$ are the longitudinal resistivities in the presence and absence of the external magnetic field, respectively. We find that $SrAl_2Si_2$ exhibits a large nonsaturating MR. The MR increases to a value of 459% at 2 K for 12 T. However, it decreases gradually with the increase of temperature and becomes 58% at 100 K for 12 T. To understand the field dependency of the MR, we have fitted the MR curve at the high field region (6 to 12 T) with the power law equation $\mathrm{MR} = \eta B^m$, where η is an arbitrary constant. The variation of m with the temperature is shown in the inset of Fig. 2(c). At very low temperatures, we find m to be nearly independent of temperature, and then it increases with temperature and reaches the value of 2 at $T = 100$ K. A more thorough analysis of the MR data reveals two other distinct features at low temperatures: quantum oscillations at high magnetic field values and WAL at low magnetic field values.

B. Shubnikov–de Haas oscillations

Quantum oscillations, namely, the Shubnikov–de Haas (SdH) oscillations, are visible from the MR data at $B > 3$ Tesla for $T \leqslant 4.5$ K. To extract the oscillatory component ($\Delta\rho_{xx}$) of the SdH oscillation in ρ_{xx}, we have subtracted a smooth polynomial background from $\rho_{xx}(B)$. The plot of $\Delta\rho_{xx}$ as a function of $1/B$ is shown in Fig. 2(d). The Fourier transformation of the SdH oscillations, as shown in Fig. 2(e), reveals a fundamental frequency $F_\gamma = 8$ T. The cross-sectional area (A_F) of the Fermi surface perpendicular to the applied field corresponding to this frequency is estimated using the Onsager relation $F = (\hbar/2\pi e)A_F$, where $\hbar$ is the reduced Planck's constant, and e is the magnitude of electron

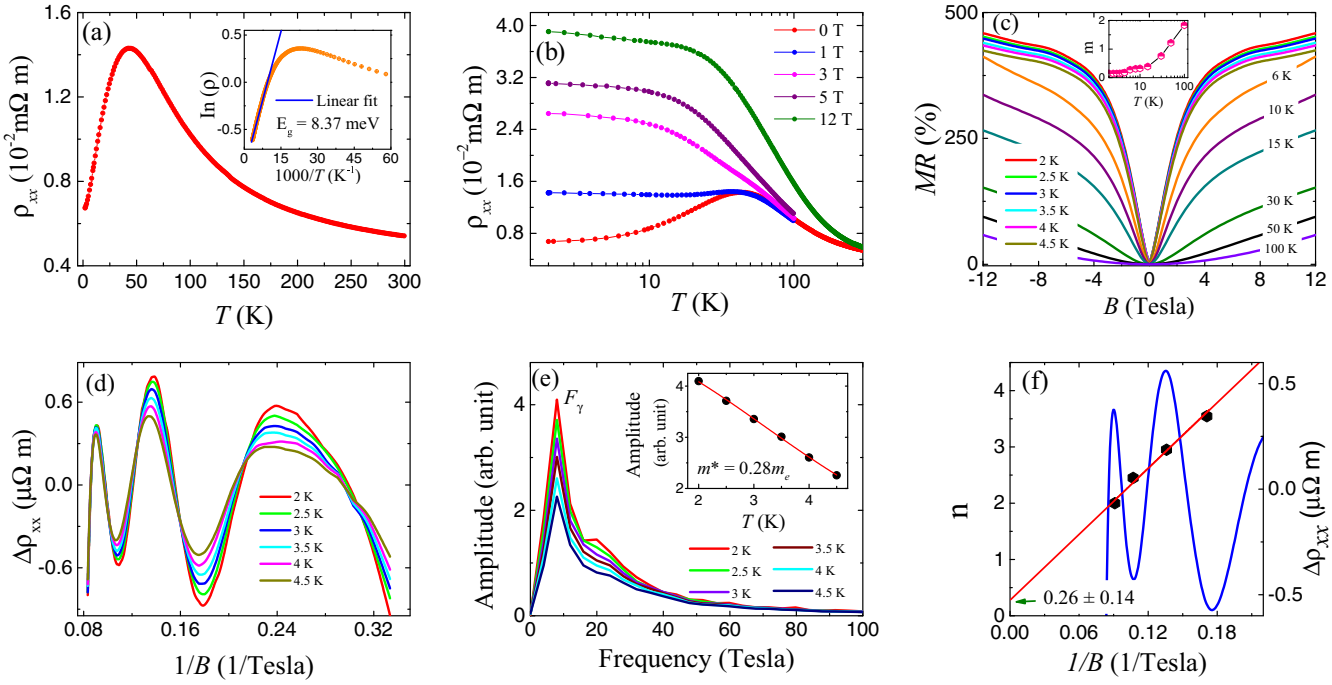

FIG. 2. Magnetotransport measurements of $SrAl_2Si_2$. (a) The temperature dependence of the longitudinal resistivity. The inset shows the fitting of the Arrhenius plot, with an activation gap of $E_g = 8.4$ meV. (b) The temperature dependence of the longitudinal resistivity in the presence of a magnetic field. (c) Magnetoresistance (MR) as a function of $B \in [-12, 12]$ Tesla for different temperatures. The inset represents the dependence of the m (MR $= \eta B^m$, where η is a constant) with T. (d) The extracted oscillatory component of the Shubnikov–de Haas (SdH) oscillations as a function of $1/B$ for temperatures between 2 and 4.5 K. (e) The fast Fourier transform (FFT) spectra of the SdH oscillations indicate a fundamental frequency $F_\gamma = 8$ Tesla. The hump near 19 T may correspond to the second harmonic. (f) The corresponding Landau level fan diagram for measurements at $T = 4$ K.

charge [7]. The estimated area (A_{F_γ}) and carrier concentration (n) corresponding to the observed frequency are 0.076 nm^{-2} and 1.28×10^{17} cm^{-3}, respectively. To determine the effective mass m^* corresponding to the frequency F_γ, we have fitted the temperature-dependent fast Fourier transform (FFT) amplitude [see inset of Fig. 2(e)] with the thermal damping factor $R_T \propto \dfrac{2\pi^2 k_B T m^*/\hbar eB}{\sinh(2\pi^2 k_B T m^*/\hbar eB)}$ of the Lifshitz-Kosovich formula, where k_B is the Boltzmann constant [30]. The fitting yields $m^* = 0.28 m_e$, where m_e is the free electron mass. A similar value of m^* was found in the sister compound $CaAl_2Si_2$ [19].

For more insight into the nature of the bands forming the Landau levels (LL), we construct the LL fan diagram from the SdH oscillations in 4 K data by specifying the LL index as integer n (half integer, $n + \frac{1}{2}$) against the conductivity maxima (minima), as shown in Fig. 2(f). We find an unequal spacing between the maxima and minima positions of the oscillation for different LLs in $SrAl_2Si_2$ [Fig. 2(d)]. A similar behavior is also found in other topological materials due to Zeeman splitting [7,31,32], which leads to an unequal energy spacing between the different LL. One can estimate the nature of the bands that contribute to the SdH oscillations from the LL fan diagram using the Lifshitz-Onsager quantization condition given by $A_F \frac{\hbar}{eB} = 2\pi(n + \gamma)$ with $\gamma = \frac{1}{2} - \beta + \delta$ [33]. Here, $2\pi\beta$ is the Berry phase which is zero for a trivial band and π for a non-trivial band. The quantity δ is the additional phase which is zero for a two-dimensional (2D) system and $\pm\frac{1}{8}$ for a three-dimensional (3D) system. For a non-trivial system, one would expect $\gamma = \pm 0.125$, and for trivial system, $\gamma = 0.625$ or 0.375 [7,33,34]. The intercept of linear fit to n vs $1/B$ plot, as shown in Fig. 2(f), gives $\gamma = 0.26 \pm 0.14$, suggesting a nonzero Berry phase ($0.45\pi \leqslant \phi_B \leqslant 1.01\pi$; considering standard error). The observed value of the Berry phase is like other non-trivial materials [35–37].

C. WAL

We now analyze another important feature observed in magnetotransport data—WAL. We find that WAL in $SrAl_2Si_2$ manifests at low magnetic field values for temperatures below $T = 15$ K [see Fig. 2(c)]. The WAL can be understood in terms of destructive quantum interference of electrons traversing different time-reversal loops. The phase shifts of electrons between two time-reversed paths can lead to either constructive or destructive interference, resulting in either weak localization or WAL, respectively. In a system with strong SOC or topologically protected bands, there is an additional π phase shift in time-reversed paths, which causes destructive interference and gives rise to negative magnetoconductivity (MC) [38–40]. The WAL correction in the MC is given by $\Delta\sigma_{xx}(B) = \sigma_{xx}(B) - \sigma_{xx}(0)$, where $\sigma_{xx}(B) = \rho_{xx}/(\rho_{xx}^2 + \rho_{yx}^2)$ is the conductivity, and ρ_{yx} is the measured Hall resistivity. We have analyzed MC data using the well-known Hikami-Larkin-Nagaoka (HLN) model. According to this model, the MC correction arising from WAL can be described as [29,41]

$$\Delta\sigma_{xx}(B) = -A\left[\Psi\left(\frac{1}{2} + \frac{\hbar}{4el_\phi^2 B}\right) - \ln\left(\frac{\hbar}{4el_\phi^2 B}\right)\right]. \quad (2)$$

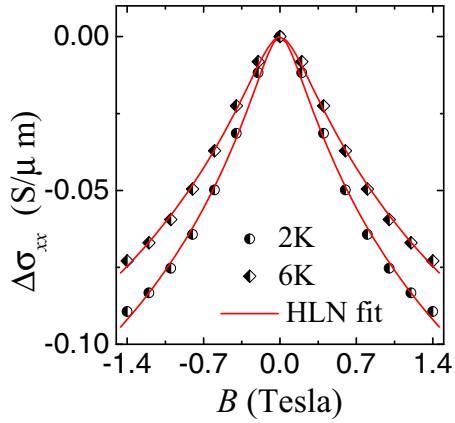

FIG. 3. The magnetoconductivity as a function of B for $T = 2$ K and for $T = 6$ K. The red solid line is the fit to the Hikami-Larkin-Nagaoka (HLN) formula specified in Eq. (2).

Here, $A = \frac{\alpha e^2}{\pi h}$, with the value of $\alpha = \frac{1}{2}$ per conduction channel for 2D materials. In Eq. (2), $\Psi(x)$ is the digamma function, and l_ϕ is the phase coherence length. We note that, even though the HLN formula was derived for 2D materials, in practice, it fits the data for 3D materials really well with large values of α. We find that the MC data for 2 and 6 K is well fitted with Eq. (2) in the low magnetic field (-1.4 T $\leqslant B \leqslant 1.4$ T) regime, as shown in Fig. 3. The estimated value of $\alpha \sim 10^6$. Such a large α value was also found in several 3D materials due to the contribution of several conduction channels [29,41–43]. The obtained l_ϕ values of 48.70 and 42.71 nm for 2 and 6 K, respectively.

D. Hall resistivity

To probe the details of the charge carriers participating in transport, we measured the Hall resistivity at different temperatures. The contribution of the MR from the Hall resistivity is eliminated using the formula $\rho_{yx}(B) = [\rho_{yx}(+B) - \rho_{yx}(-B)]/2$. The obtained non-linear Hall resistivity is shown in Fig. 4, with a clear signature of both electrons and holes participating in the magnetotransport. The Hall conductivity is obtained from the symmetrized $\rho_{yx}(B)$, using the relation $\sigma_{xy}(B) = \rho_{yx}/(\rho_{xx}^2 + \rho_{yx}^2)$. To quantify the contributions of the holes and electrons in the observed Hall conductivity and longitudinal conductivity, we fitted our measured data with the two-carrier model of $\sigma_{xy}(B)$ and σ_{xx}(B), respectively (see Fig. 4), which is given by [19]

$$\sigma_{xy}(B) = eB\left[\frac{n_h\mu_h^2}{1+(\mu_h B)^2} - \frac{n_e\mu_e^2}{1+(\mu_e B)^2}\right], \quad (3)$$

$$\sigma_{xx}(B) = e\left[\frac{n_h\mu_h}{1+(\mu_h B)^2} + \frac{n_e\mu_e}{1+(\mu_e B)^2}\right]. \quad (4)$$

Here, n_h and n_e (μ_h and μ_e) denote the carrier concentration (mobility) of the holes and the electrons, respectively. The extracted values of carrier concentration and mobility from the fitted curves $\sigma_{xy}(B)$ and $\sigma_{xx}(B)$ are comparable and exhibit similar temperature dependence, as presented in Fig. 5. At low temperatures, the estimated $n_e \sim 10^{17}$ cm^{-3} and $n_h \sim 10^{18}$ cm^{-3}, which increase as the temperature rises. On the other hand, at low temperatures, $\mu_e \sim 10^2$ cm^2 V^{-1} S^{-1} and $\mu_h \sim 10^4$ cm^2 V^{-1} S^{-1}. Electron mobility decreases

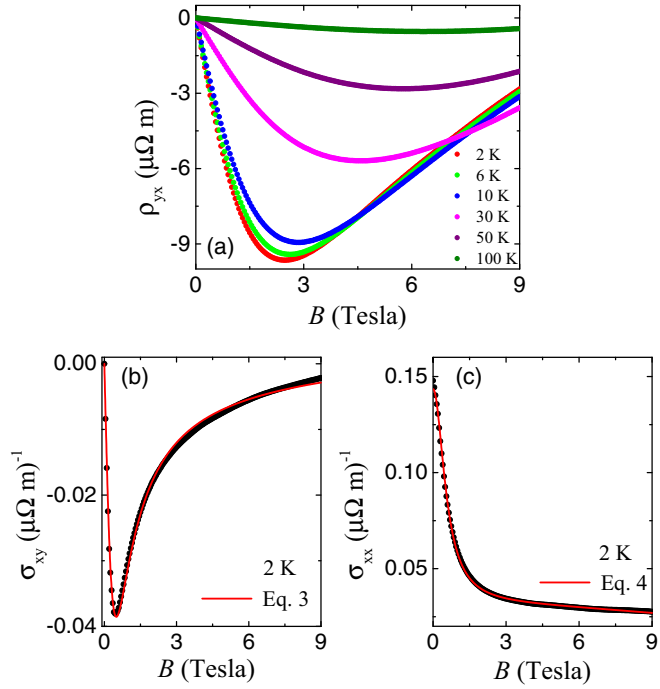

FIG. 4. (a) Hall resistivity measured at different temperatures. (b) Hall conductivity (σ_{xy}) and (c) longitudinal conductivity (σ_{xx}) as a function of the magnetic field at 2 K. The solid red line is the fitting of the two-band model as presented in Eqs. (3) and (4).

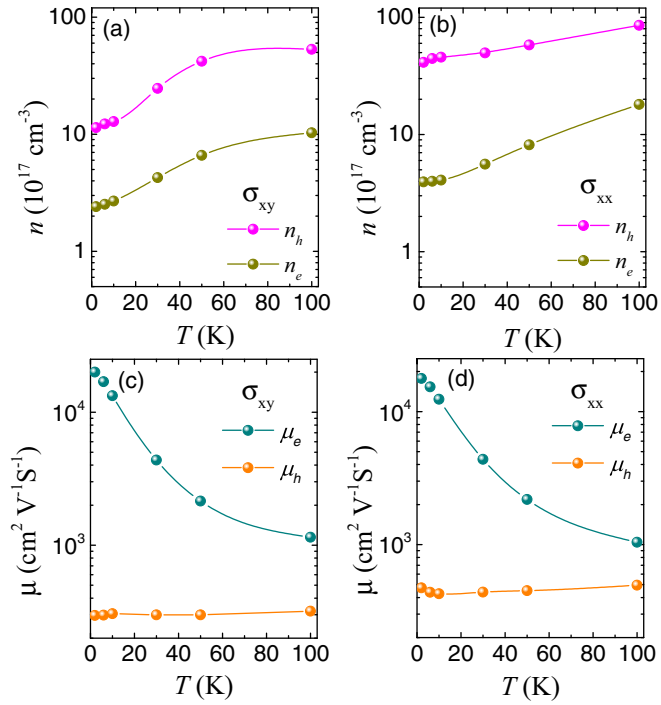

FIG. 5. The variation of carrier concentration and mobility with temperature. (a) and (b) Estimated carrier concentrations from Eqs. (3) and (4), respectively. (c) and (d) Calculated mobilities using Eqs. (3) and (4), respectively.

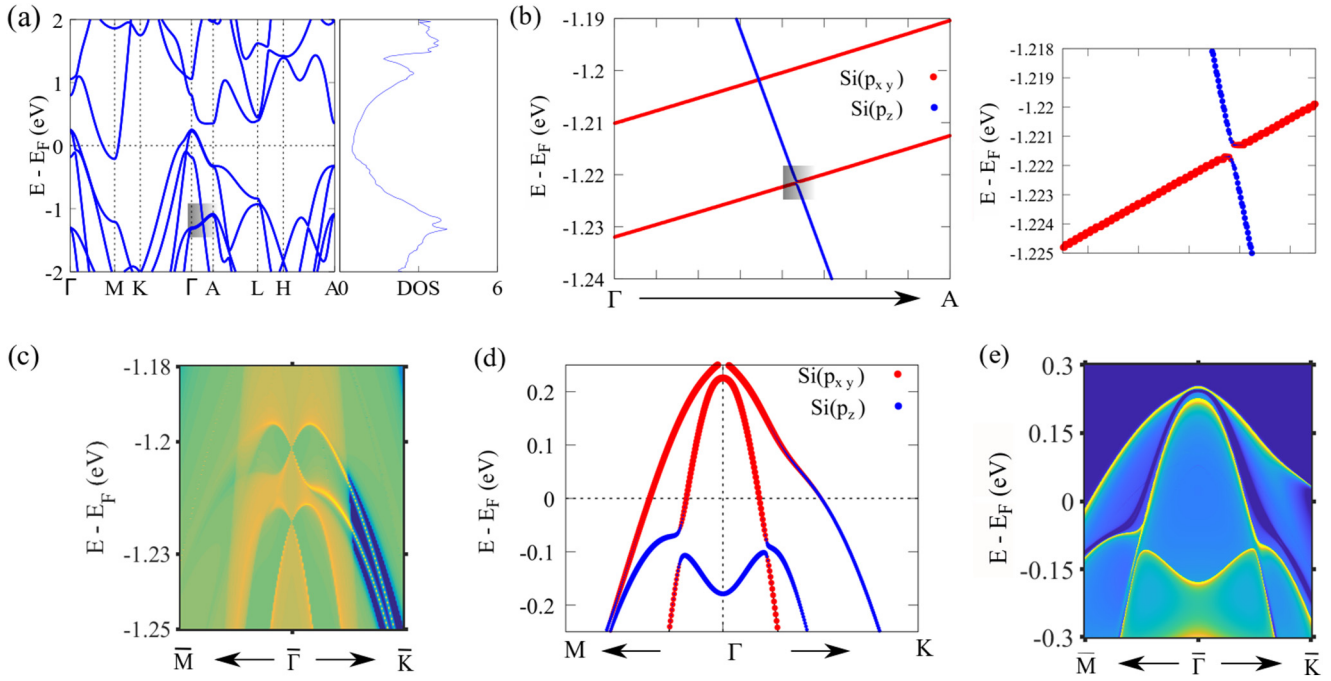

FIG. 6. The band structure and surface states including spin-orbit coupling (SOC). (a) The bulk band structure along different high-symmetry directions along with the total density of states. (b) Zoomed-in band structure along the Γ-*A* direction with orbital character. The band inversion between Si p_{xy} and p_z orbitals at $E \approx -1.22$ eV is shown separately in the side panel. The Dirac crossing and the inverted bandgap seen here give rise to topological surface states, as shown in (c). (d) Band inversion near the Fermi energy along the *M*-Γ-*K* direction. Thus, the inverted bandgap turns out to be topologically trivial, and it is not associated with Dirac-like topological surface states, as shown in (e).

monotonically as temperature increases, whereas hole mobility is nearly temperature independent. The low carrier concentration and relatively large mobility is also observed in several other topological materials [7,44]. The obtained carrier concentration suggests that $SrAl_2Si_2$ is an uncompensated material. Thus, in contrast to other topological systems [7,45,46], the large MR in $SrAl_2Si_2$ may not arise from electron-hole compensation.

IV. ELECTRONIC STRUCTURE

To understand the electronic properties of $SrAl_2Si_2$ better, we now calculate its bulk band structure in the presence of SOC, and it is shown in Fig. 6(a). Clearly, the valence band crosses the Fermi energy near the Γ point, giving rise to a hole pocket, and the conduction band crosses the Fermi level in the vicinity of the *M* point, creating an electron pocket. A pair of Dirac-like crossings in the bulk bands can be seen along the Γ-*K* direction for $E \approx -0.1$ eV. Another tilted type-I Dirac crossing along the Γ-*A* direction can be observed for $E \approx -1.2$ eV, as shown in Fig. 6(b). Moreover, a band inversion between Si p_{xy} and p_z orbitals with a small gap can be observed at $E \approx -1.22$ eV in the zoomed region of Fig. 6(b).

To explore the topological nature of this band inversion, we have calculated the surface states for the (001) surface. Distinct Dirac-like gapless surface states can be observed at $E \approx -1.20$ eV and -1.22 eV, as shown in Fig. 6(c). We also calculate the surface states to explore the band inversion [shown in Fig. 6(d)] near the Fermi energy. However, no distinct surface states arising from the band inversion in the vicinity of $E \approx -0.10$ eV can be seen in Fig. 6(e), indicating its topologically trivial nature. These features clearly indicate that $SrAl_2Si_2$ hosts a type-I topological Dirac semimetal state along with a topological band inversion arising from the band features along the Γ-*A* direction. In addition to these, very clear and high intensity surface states can also be seen in Fig. 6(e), which may arise from a topological band inversion in the conduction band at $E \approx 0.2$ eV but which have finite contributions at the Fermi energy. Similar band features have also been observed in other iso-structure compounds [7,19,45,46].

Along with these, the band structure also hosts a pair of hole pocket (labeled H_1 and H_2) at the Γ point and an electron pocket (E_1) at the *M* point. To explore the structure of these charge carrier pockets, we calculate the Fermi surfaces (with SOC) over the 3D BZ in Figs. 7(a) and 7(b). A closed set of electron pockets around the *M* point and a closed pair of hole pockets around the Γ point can be clearly seen [pocket H_1 in panel (a) and pocket H_2 in panel (b)]. Figures 7(c) and 7(d) show the constant energy contours in the (001) surface-projected spectral function for different binding energies. These capture the bulk projected Fermi surfaces along with the topological surface states. On decreasing the Fermi energy, the hole pockets near the Γ point expand, whereas the electron pockets at the *M* point decrease in size, confirming our interpretation. The presence of both the hole and electron pockets is consistent with our two-carrier-model-based fit for the observed Hall resistivity.

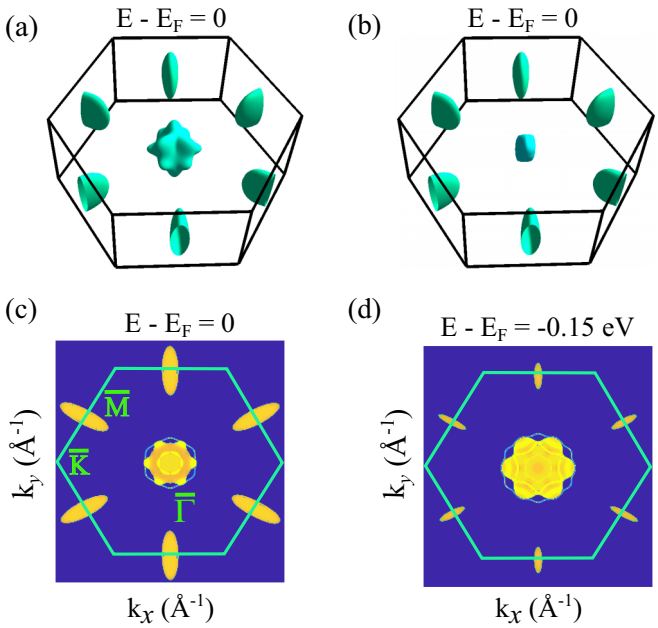

FIG. 7. The bulk and surface projected Fermi surface. The bulk Fermi surface [including spin-orbit coupling (SOC)] showing the electron pockets around the M point, and (a) only the H_1 hole pocket and (b) the smaller H_2 hole pocket at the center of the Brillioun zone (BZ). (c) and (d) The constant energy contours of the (001) surface-projected spectral function for energy values $E - E_F = 0$ and -0.15 eV, respectively. On decreasing the energy below the Fermi level, the shrinking of the electron pockets, the growth of the hole pockets, and the change in the surface states can be clearly seen.

V. DISCUSSION

Previous measurements reveal that $SrAl_2Si_2$ possesses a pseudogap with rapidly changing density of states (with energy) in the vicinity of the Fermi energy. Additionally, the sharp band feature hosting the electron and hole pockets can be smeared out by changing the densities of electronic carriers, which have direct influence on the resistivity peak [47]. Thus, the appearance of a resistivity anomaly can be attributed to the presence of two different charge carriers whose density can change with temperature [27,47]. With the application of the magnetic field, the low-temperature resistivity value gets enhanced, leading to a resistivity plateau. The appearance of a resistivity plateau on the application of a magnetic field is also observed in other TSMs [7,43,48,49]. The observed large nonsaturating MR in $SrAl_2Si_2$ is comparable with that observed in other TSMs [50–52].

The typical mechanisms that leads to large non-saturation MR in TSMs are perfect charge carriers compensation, the non-trivial topological state and a combined effect of a large difference between electron and hole mobility with a moderate carrier compensation [53]. In our case, the unequal carrier concentration measured from Hall effect rule out the possibility of charge compensation. The theoretically estimated shapes and volumes of the Fermi surfaces also indicate the uncompensated nature of the charge carrier. The uncompensated nature of the charge carriers should reflect in the quadratic variation of MR with B. However due to the dominant WAL effect at lower temperature, a quasilinear dispersion is observed. On increasing the temperature, the WAL effect gets suppressed and the dependence of MR moves toward quadratic. There is a type-I Dirac band crossing in $SrAl_2Si_2$, but it is far below the Fermi level (≈ -1.2 eV). Thus, the contribution of Dirac Fermion to the magneto-transport, which is a Fermi surface property, is likely to be insignificant. The large value of MR in $SrAl_2Si_2$ is neither related to the charge carrier compensation nor due to non-trivial band topology. Thus, we believe the large MR in $SrAl_2Si_2$ arises from combination of moderate charge carrier compensation and substantial difference between electron and hole mobilities. A relatively large MR originating from similar phenomena was reported earlier in other semimetals, such as YSb and SiP_2 [53,54].

VI. CONCLUSIONS

In conclusion, we have performed a systematic study on a good quality single crystal of $SrAl_2Si_2$ by magnetotransport measurement and band structure calculations. Electrical transport data resemble that of metals and semiconductors at low and high temperatures, respectively. The observed large nonsaturating MR and resistivity plateaus are like that observed in other TSMs. The WAL effect is unveiled by analyzing MC data with the HLN model. The measured Hall resistivity is nonlinear in B, and fits well with the two-carrier model, confirming the presence of both electrons and holes as charge carriers. Our band structure calculation suggests that $SrAl_2Si_2$ is a topologically non-trivial material with type-I tilted Dirac fermions in addition to other topological band inversions.

ACKNOWLEDGMENTS

We acknowledge IIT Kanpur, Science and Engineering Research Board (SRG/2019/001686 and CRG/2018/000220), IIT Roorkee (SMILE-13), and the Department of Science and Technology for financial support. We acknowledge the High Performance Computing facility at IIT Kanpur, for computational support.

[1] M. Z. Hasan and C. L. Kane, Rev. Mod. Phys. **82**, 3045 (2010).
[2] N. P. Armitage, E. J. Mele, and A. Vishwanath, Rev. Mod. Phys. **90**, 015001 (2018).
[3] Z. K. Liu, B. Zhou, Y. Zhang, Z. J. Wang, H. M. Weng, D. Prabhakaran, S.-K. Mo, Z. X. Shen, Z. Fang, X. Dai *et al.*, Science **343**, 864 (2014).
[4] A. Mosca Conte, O. Pulci, and F. Bechstedt, Sci. Rep. **7**, 45500 (2017).
[5] J. Nayak, S.-C. Wu, N. Kumar, C. Shekhar, S. Singh, J. Fink, E. E. D. Rienks, G. H. Fecher, S. S. P. Parkin, B. Yan *et al.*, Nat. Commun. **8**, 13942 (2017).
[6] G. Bian, T.-R. Chang, R. Sankar, S.-Y. Xu, H. Zheng, T. Neupert, C.-K. Chiu, S.-M. Huang, G. Chang, I. Belopolski *et al.*, Nat. Commun. **7**, 10556 (2016).
[7] R. Singha, A. K. Pariari, B. Satpati, and P. Mandal, Proc. Natl. Acad. Sci. USA **114**, 2468 (2017).

[8] K. Kuroda, T. Tomita, M.-T. Suzuki, C. Bareille, A. A. Nugroho, P. Goswami, M. Ochi, M. Ikhlas, M. Nakayama, S. Akebi *et al.*, Nat. Mater. **16**, 1090 (2017).

[9] H. Li, H.-W. Wang, Y. Li, H. Zhang, S. Zhang, X.-C. Pan, B. Jia, F. Song, and J. Wang, Nano Lett. **19**, 2450 (2019).

[10] A. Laha, P. Rambabu, V. Kanchana, L. Petit, Z. Szotek, and Z. Hossain, Phys. Rev. B **102**, 235135 (2020).

[11] B. Ghosh, D. Mondal, C.-N. Kuo, C. S. Lue, J. Nayak, J. Fujii, I. Vobornik, A. Politano, and A. Agarwal, Phys. Rev. B **100**, 195134 (2019).

[12] B. Singh, B. Ghosh, C. Su, H. Lin, A. Agarwal, and A. Bansil, Phys. Rev. Lett. **121**, 226401 (2018).

[13] B. Singh, S. Mardanya, C. Su, H. Lin, A. Agarwal, and A. Bansil, Phys. Rev. B **98**, 085122 (2018).

[14] L.-L. Wang, N. H. Jo, B. Kuthanazhi, Y. Wu, R. J. McQueeney, A. Kaminski, and P. C. Canfield, Phys. Rev. B **99**, 245147 (2019).

[15] J.-Z. Ma, S. M. Nie, C. J. Yi, J. Jandke, T. Shang, M. Y. Yao, M. Naamneh, L. Q. Yan, Y. Sun, A. Chikina *et al.*, Sci. Adv. **5**, eaaw4718 (2019).

[16] J.-R. Soh, F. de Juan, M. G. Vergniory, N. B. M. Schröter, M. C. Rahn, D. Y. Yan, J. Jiang, M. Bristow, P. Reiss *et al.*, Phys. Rev. B **100**, 201102(R) (2019).

[17] H. Su, B. Gong, W. Shi, H. Yang, H. Wang, W. Xia, Z. Yu, P.-J. Guo, J. Wang, L. Ding *et al.*, APL Mater. **8**, 011109 (2020).

[18] M. C. Rahn, J.-R. Soh, S. Francoual, L. S. I. Veiga, J. Strempfer, J. Mardegan, D. Y. Yan, Y. F. Guo, Y. G. Shi, and A. T. Boothroyd, Phys. Rev. B **97**, 214422 (2018).

[19] H. Su, X. Shi, W. Xia, H. Wang, X. Hanli, Z. Yu, X. Wang, Z. Zou, N. Yu, W. Zhao *et al.*, Phys. Rev. B **101**, 205138 (2020).

[20] T. Deng, C. Chen, H. Su, J. He, A. Liang, S. Cui, H. Yang, C. Wang, K. Huang, C. Jozwiak *et al.*, Phys. Rev. B **102**, 045106 (2020).

[21] G. Kresse and J. Furthmüller, Phys. Rev. B **54**, 11169 (1996).

[22] G. Kresse and D. Joubert, Phys. Rev. B **59**, 1758 (1999).

[23] J. P. Perdew, K. Burke, and M. Ernzerhof, Phys. Rev. Lett. **77**, 3865 (1996).

[24] H. J. Monkhorst and J. D. Pack, Phys. Rev. B **13**, 5188 (1976).

[25] N. Marzari and D. Vanderbilt, Phys. Rev. B **56**, 12847 (1997).

[26] Q. Wu, S. Zhang, H.-F. Song, M. Troyer, and A. A. Soluyanov, Comput. Phys. Commun. **224**, 405 (2018).

[27] S. M. Kauzlarich, C. L. Condron, J. K. Wassei, T. Ikeda, and G. J. Snyder, J. Solid State Chem. **182**, 240 (2009).

[28] C. P. Fang, C. S. Lue, and B.-L. Young, Phys. Rev. B **83**, 113105 (2011).

[29] Z. Hou, Y. Wang, G. Xu, X. Zhang, E. Liu, W. Wang, Z. Liu, X. Xi, W. Wang, and G. Wu, Appl. Phys. Lett. **106**, 102102 (2015).

[30] D. Shoenberg, *Magnetic Oscillations in Metals*, Cambridge Monographs on Physics (Cambridge University Press, Cambridge, 1984).

[31] J. Hu, J. Y. Liu, D. Graf, S. M. A. Radmanesh, D. J. Adams, A. Chuang, Y. Wang, I. Chiorescu, J. Wei, L. Spinu *et al.*, Sci. Rep. **6**, 18674 (2016).

[32] L. Xing, R. Chapai, R. Nepal, and R. Jin, npj Quantum Mater. **5**, 10 (2020).

[33] M. Busch, O. Chiatti, S. Pezzini, S. Wiedmann, J. Sánchez-Barriga, O. Rader, L. V. Yashina, and S. F. Fischer, Sci. Rep. **8**, 485 (2018).

[34] T. A. Romanova, D. A. Knyazev, Z. Wang, A. V. Sadakov, and V. A. Prudkoglyad, Phys. B: Condens. Matter **536**, 43 (2018).

[35] W. Xia, X. Shi, Y. Wang, W. Ge, H. Su, Q. Wang, X. Wang, N. Yu, Z. Zou, Y. Hao *et al.*, Appl. Phys. Lett. **116**, 142103 (2020).

[36] O. Pavlosiuk and D. Kaczorowski, Sci. Rep. **8**, 11297 (2018).

[37] A. Pariari, P. Dutta, and P. Mandal, Phys. Rev. B **91**, 155139 (2015).

[38] G. Bergmann, Solid State Commun. **42**, 815 (1982).

[39] G. Bergmann, Phys. Rep. **107**, 1 (1984).

[40] H. Hayasaka and Y. Fuseya, J. Phys.: Condens. Matter **32**, 16LT01 (2020).

[41] S. Malick, A. Ghosh, C. K. Barman, A. Alam, Z. Hossain, P. Mandal, and J. Nayak, Phys. Rev. B **105**, 165105 (2022).

[42] J. Zhang, Z. Hou, C. Zhang, J. Chen, P. Li, Y. Wen, Q. Zhang, W. Wang, and X. Zhang, Appl. Phys. Lett. **115**, 172407 (2019).

[43] A. Laha, S. Malick, R. Singha, P. Mandal, P. Rambabu, V. Kanchana, and Z. Hossain, Phys. Rev. B **99**, 241102(R) (2019).

[44] C.-Z. Li, J.-G. Li, L.-X. Wang, L. Zhang, J.-M. Zhang, D. Yu, and Z.-M. Liao, ACS Nano **10**, 6020 (2016).

[45] A. Wang, D. Graf, Y. Liu, Q. Du, J. Zheng, H. Lei, and C. Petrovic, Phys. Rev. B **96**, 121107(R) (2017).

[46] J. Wang, L. Li, W. You, T. Wang, C. Cao, J. Dai, and Y. Li, Sci. Rep. **7**, 15669 (2017).

[47] C. Lue, C. Fang, A. Abhyankar, J. Lin, H. Lee, C. Chang, and Y. Kuo, Intermetallics **19**, 1448 (2011).

[48] F. F. Tafti, Q. D. Gibson, S. K. Kushwaha, N. Haldolaarachchige, and R. J. Cava, Nat. Phys. **12**, 272 (2016).

[49] Y.-Y. Wang, Q.-H. Yu, P.-J. Guo, K. Liu, and T.-L. Xia, Phys. Rev. B **94**, 041103(R) (2016).

[50] O. Pavlosiuk, P. Swatek, and P. Wiśniewski, Sci. Rep. **6**, 38691 (2016).

[51] S. Sasmal, R. Mondal, R. Kulkarni, A. Thamizhavel, and B. Singh, J. Phys.: Condens. Matter **32**, 335701 (2020).

[52] A. Laha, S. Mardanya, B. Singh, H. Lin, A. Bansil, A. Agarwal, and Z. Hossain, Phys. Rev. B **102**, 035164 (2020).

[53] J. He, C. Zhang, N. J. Ghimire, T. Liang, C. Jia, J. Jiang, S. Tang, S. Chen, Y. He, S.-K. Mo *et al.*, Phys. Rev. Lett. **117**, 267201 (2016).

[54] Y. Zhou, Z. Lou, S. Zhang, H. Chen, Q. Chen, B. Xu, J. Du, J. Yang, H. Wang, C. Xi *et al.*, Phys. Rev. B **102**, 115145 (2020).